Macromolecules

pubs.acs.org/Macromolecules
Article

Core–Shell Nanogels With Raspberry Architecture and Amine Loading in the Core via Precipitation Polymerization: A Mechanistic Study

Bruno Espuche, Krishan Kumar, Paolo Moretti, Maria Grazia Ortore, Olena Ivashchenko, Emerson Coy, Heinz Amenitsch, Sergio E. Moya,* and Marcelo Calderón*

Cite This: *Macromolecules* 2024, 57, 6035–6048

ABSTRACT: Nanogels (NGs) are synthesized by precipitation polymerization of dendritic polyglycerol (dPG), *N*-isopropylacrylamide (NIPAM), and *N*-isopropyl methacrylamide (NIPMAM). The stabilization and agglomeration of subunits during the NG growth result in raspberry-like structures, as shown by transmission electron microscopy, atomic force microscopy, and small-angle X-ray scattering measurements. Positive charges are introduced into dPG-NIPAM-NIPMAM NGs by (1) the copolymerization of dimethylaminoethyl methacrylate (DMAEMA) and (2) the copolymerization of glycidyl methacrylate (GMA), followed by its functionalization with ethylenediamine (ED) through the epoxy group. Homogeneous structures are obtained by the copolymerization in batch of DMAEMA with the other monomers, whereas core–shell NGs are reached by semibatch copolymerization of GMA. After amination, the charges are restricted to the core of the NGs.

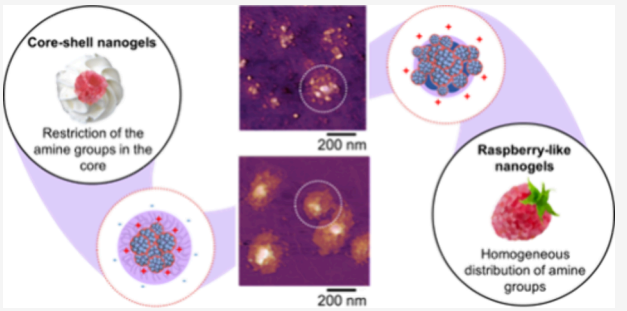

INTRODUCTION

In the last decades, great attention has been given to polymeric nanoparticles for advanced applications.[1−5] For instance, nanogels (NGs), i.e., highly hydrated cross-linked nanosized polymeric particles, have become a rising star in nanomedicine for the delivery of therapeutics and small drugs.[6−11] Their nanometric size, stability, softness, and swelling behavior are assets for the safe and controlled encapsulation and release of cargos.[12] Inspired by the great potential of gene therapy to prevent, treat, and cure many diseases, polycationic NGs have been developed to complex negatively charged nucleic acids and deliver them inside targeted cells.[9,10] Although considerable achievements have been made in this field, the therapeutic window of NGs for gene delivery remains narrow. Positive charges, which are needed for nucleic acid complexation and transfection, are also responsible for toxicological end points.[13−15] Core–shell NGs with positive charges selectively placed in the core have been tested for gene delivery with encouraging results, mostly regarding the decrease in cytotoxicity.[16−18] In order to enlarge the therapeutic window of NGs, i.e., optimize the transfection efficiency and the cytocompatibility, advanced structures with a high level of control in the location of positive charges are required.[19] To produce such NGs, a deep understanding of the polymerization pathways is demanded.

Precipitation polymerization is a polymerization technique frequently reported for the synthesis of NGs.[20] This technique is based on the difference in solubility between the monomers and the growing polymers: when the chain length of the polymers increases, their solubility decreases resulting in their condensation into nanoparticles.[21] When cross-linkers are introduced in the synthesis, covalent linking between chains takes place, forming the NGs. High control in the nanoparticle size, low dispersity, and low surfactant concentrations are advantages of precipitation polymerization over other techniques, such as emulsion polymerization. Precipitation polymerization is particularly suitable for the synthesis of NGs with intricate structures. For example, NGs with core–shell structures via a two-step precipitation method have been reported by this technique.[22−24] Following this method, small NGs were first synthesized and used as nuclei to grow a shell around the nuclei in a second precipitation step.

Responsive NGs arise due to the sensitivity of certain polymers to stimuli, including changes in pH, temperature, redox conditions, or the presence of enzymes.[25,26] Responsive NGs can collapse, swell, and degrade by the application of a

Received: February 9, 2024
Revised: May 1, 2024
Accepted: June 4, 2024
Published: June 11, 2024

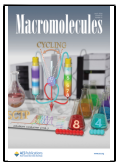

https://doi.org/10.1021/acs.macromol.4c00350
Macromolecules 2024, 57, 6035−6048

controlled trigger. Nanomedicine has taken advantage of these smart tools for the controlled release of therapeutic cargos. For example, thermoresponsive NGs based on dendritic polyglycerol (dPG) and poly(*N*-isopropylacrylamide) (P(NIPAM)) have already been investigated for protein encapsulation.[27,28] P(NIPAM) is one of the most reported thermoresponsive polymers, with a lower critical solution temperature (LCST) of around 32 °C, and dPG is a highly biocompatible molecule that can be modified and used as a cross-linker. dPG displays a high density of hydroxyl and ester groups, providing high water solubility and low cytotoxic profiles for the resulting NGs. The synthesis of acrylated dPG permits a good control in the acrylation degree, allowing to finely tune the swelling ratio and the size of the inner pores.[29] Due to both structural tunability and biocompatibility, the NGs based on dPG are attractive in biomedical applications. dPG-NIPAM NGs can achieve controlled delivery of proteins by loading them when swelling and expelling them when collapsing above the transition temperature.[27,28] Differently from protein delivery, no studies of thermocontrolled release of nucleic acid for gene delivery applications have been reported. In most nonviral carriers, electrostatic interactions are the main forces used for loading nucleic acids. Yet, the thermoinduced swelling and collapsing of charged NGs do not directly affect electrostatic interactions, since the charges of both the cargo and the vector remain unaffected during the change in the hydration degree. However, the density and location of the amine moieties can be altered to become inaccessible for complexation.[30] For that, the polymeric organization and the location of the complexation points must be finely controlled.

With the aim of designing suitable thermoresponsive NGs for nucleic acid delivery with low toxicity, we explored in this work the fabrication of core−shell NGs on the basis of the copolymerization of NIPAM, *N*-isopropyl methacrylamide (NIPMAM), and dPG. NIPMAM was introduced as a comonomer to increase the volume phase transition temperature (VPTT) of dPG-P(NIPAM) NGs above physiological values.[29,31] By strategically choosing a VPTT higher than normal body temperature, these NGs consistently maintained a swollen state under physiological conditions. This characteristic becomes advantageous in scenarios needing externally triggered responses such as drug release activated by localized hyperthermia. First, the precipitation growth mechanism was investigated, and the morphology of the NGs was elucidated by electron and atomic force microscopy. Here, the importance of dPG in the stabilization of subunits within the growing NG was highlighted. Then, positive charges were incorporated into the dPG-P(NIPAM)-P(NIPMAM) NGs through two strategies: (1) the copolymerization of dimethylaminoethyl methacrylate (DMAEMA); (2) the copolymerization of glycidyl methacrylate (GMA) with successive functionalization with ethylene diamine (ED) via the reactive epoxy group. These two monomers were chosen because of their differences in hydrophilicity: P(DMAEMA) is known to be relatively hydrophilic, whereas P(GMA) is a hydrophobic polymer. We hypothesized that GMA's hydrophobicity, along with its high reactivity, promotes its precipitation into the core of the NGs. Indeed, while hydrophilic segments tend to stay on the surface to stabilize the growing nanoparticles in water, relatively hydrophobic oligoradicals tend to condense in the core. Thereby, core−shell NGs could be obtained by a one-step synthesis. Then, after functionalization with ED, the positive charges should all be located within the core of the NGs. Batch and semibatch precipitation copolymerization were achieved with DMAEMA and GMA NGs to test the precipitation limits in hydrophilic and hydrophobic systems. Finally, both pH- and thermoresponsiveness of the NGs were evaluated. Unique thermal behavior was obtained with the core−shell NGs, with a change in surface charge from negative to positive values when crossing the transition temperature of the NGs. Overall, the work presented here brings advanced understanding of the architecture of the NGs synthesized via batch and semibatch routes, and of their physicochemical characteristics.

EXPERIMENTAL SECTION

Materials and Methods. Dendritic polyglycerol (dPG) with an average molecular weight of 9 kDa was obtained from Nanopartica GmbH. Acryloyl chloride (97%), triethylamine (99%), *N*-isopropylacrylamide (NIPAM, 99%), *N*-isopropyl methacrylamide (NIPMAM, 97%), 2-(dimethylamino)ethyl methacrylate (DMAEMA, 98%), glycidyl methacrylate (GMA, 97%), ethylenediamine (ED, ≥ 99%), ammonium persulfate (APS, ≥ 98%), sodium dodecyl sulfate (SDS, ≥ 98%), hydroquinone (≥99%), *N*,*N*-dimethylformamide (DMF, ≥ 99%), and deuterium oxide (D_2O, 99.9 D atom%) were purchased from Sigma-Aldrich, VWR, and Scharlab. Water was purified into milli-Q grade using a Vent Filter from Merck. Reaction temperatures were monitored using oil baths and an MR Hei-Tec magnetic stirrer from Heidolph. NGs were freeze-dried over 3 days in a Telstar LyoQuest lyophilizer programmed at −80 °C and 0.02 mbar.

Synthesis of Acrylated dPG. The synthesis of dPG with a controlled acrylic group number (dPG-acryl) has already been published elsewhere. Here, dPG-acryl with 10% acrylation of the total available OH groups was used in the synthesis of all of the NGs. In brief, dPG (9 kDa) was subjected to overnight drying, followed by dissolution in DMF at a concentration of 50 mg/mL. To achieve 10% acrylation, TEA and acryloyl chloride were added in respective molar equivalents of 0.2 and 0.15 with respect to the free OH groups of dPG, under stirring at 0 °C. Following the final dropwise addition of acryloyl chloride, the solution was removed from the ice bath and stirred overnight at room temperature. Subsequently, purification was carried out through dialysis in methanol followed by water using a cellulose membrane with a molecular weight cutoff (MWCO) of 50 kDa. The acrylation conversion of 9.7% of the hydroxyl groups was confirmed using ^{1}H nuclear magnetic resonance (NMR) spectroscopy (Figure S1). ^{1}H NMR (298 K, 300 MHz, H_20): δ = 3.0−4.5 (m, 5H, polyglycerol protons), 5.7−6.6 (m, 3H, acrylic groups).

Synthesis of dPG-P(NIPAM)-P(NIPMAM) NGs. dPG-P(NIPAM)-P(NIPMAM) NGs, here named control NGs (C-NG), were prepared via batch precipitation polymerization, with slight modifications from previous reports.[28,32] 33 mg of dPG-acryl 10%, 50 mg of NIPAM, 50 mg of NIPMAM, 1.8 mg of SDS, and 2.8 mg of APS were mixed in 5 mL of water, and the solution was degassed with argon for 10 min. The polymerization was achieved by stirring the solution at 68 °C for 4 h. Subsequently, purification was carried out by dialysis against water using a cellulose membrane with a MWCO of 50 kDa. Following purification, the product was freeze-dried, resulting in the formation of a solid with a cotton-like appearance. Yield: 91%. FTIR: ν (cm^{-1}) = 3100−3700 (O−H, dPG), 2971, 2931, 2874, 1732 (C═O, dPG acrylation ester), 1635 (C═O amide, NIPAM, and NIPMAM), 1525 (C═O, amide, NIPAM, and NIPMAM), 1457, 1387 (C−H isopropyl group, NIPAM, and NIPMAM), 1366 (C−H isopropyl group, NIPAM, and NIPMAM), 1220, 1173, 1129, 1077, 965, 927, 884, 840. ^{1}H NMR: (300 MHz, D_2O), δ (ppm): 0.9 (s, 3H, methyl group of NIPMAM), 1.1 (s, 6H, isopropyl groups of NIPAM and NIPMAM), 0.8−2.4 (m, 3H polymer backbone NIPAM + 2H polymer backbone NIPMAM), 3.3−4.3 (7H, polyglycerol scaffold protons +1H NIPAM + 1H NIPMAM). FTIR and ^{1}H NMR spectra are shown in Figures S2 and S3.

Synthesis of DMAEMA and GMA NGs via Batch Synthesis. Copolymerization of DMAEMA and GMA with dPG, NIPAM and NIPMAM was conducted under similar batch conditions as previously

https://doi.org/10.1021/acs.macromol.4c00350
Macromolecules 2024, 57, 6035−6048

described and reported in the literature.[27] 100 mg of a mixture of NIPAM, NIPMAM, and DMAEMA or GMA were mixed with 33 mg of dPG-acryl 10%, 1.8 mg of SDS, and 2.8 mg of APS in 5 mL of water. Monomer mass ratios of 5, 10, and 20% of DMAEMA (DMAEMA B-NG 5, 10, 20) or GMA (GMA B-NG 5, 10 and 20) were fed to the reaction (quantities in Tables S1 and S2). To facilitate the dissolution of GMA, the mixture was subjected to ultrasonication for a brief period. Subsequently, the solution was degassed with argon for 10 min before initiating the polymerization process, which involved stirring at 68 °C. Following a reaction time of 5 h, purification was performed by dialyzing the solution against water using a cellulose membrane with a MWCO of 50 kDa. After purification, the product was freeze-dried, yielding a cotton-like solid. Yields of DMAEMA B-NG: 70−91%. Yields of GMA B-NG: 95−97%.

Synthesis of DMAEMA and GMA NGs via Semibatch Synthesis. Respective semibatch copolymerization of DMAEMA (DMAEMA SB-NG 5, 10, 20) and GMA (GMA SB-NG 5, 10 and 20) were carried out with the same quantities as for batch reactions (Table S1) but with slow addition of NIPAM and NIPMAM monomers. For that, dPG, DMAEMA or GMA, APS, and SDS were mixed in 4 mL of water. In the case of the GMA SB-NG synthesis, the solution was subjected to ultrasonication for a brief duration to facilitate GMA dissolution. Subsequently, the solution was degassed with argon for 10 min, and the reaction was initiated by stirring at 68 °C. Concurrently, a 2 mL aqueous solution of NIPAM and NIPMAM was continuously added to the reaction mixture using a syringe pump over a period of 1 h. Throughout this duration, the solution was maintained under an argon atmosphere. After the 6 h reaction, purification is carried out by dialysis against water using a cellulose membrane with a MWCO of 50 kDa. After purification, the product was freeze-dried, yielding a cotton-like solid. Yields of DMAEMA SB-NG: 30−38%. Yields of GMA SB-NG: 62−88%.

Synthesis of ED-GMA B-NG and SB-NG. The functionalization of GMA with ED was achieved directly after the purification of GMA B-NG (ED-GMA B-NG) and GMA SB-NG (ED-GMA SB-NG). For all GMA NGs, half of the purified solution was transferred from the dialysis membrane to a round-bottom flask with 10 mL of DMF and 10 equiv of ED relative to the epoxy groups. The reaction was allowed to proceed for 48 h at 60 °C with continuous stirring. After purification, the product was freeze-dried, yielding a cotton-like solid. Yield of functionalization: 3−5%.

Characterizations. The reaction yields of the NGs were quantified by gravimetric measurements after purification and lyophilization of the NGs using a QUINTIX 125D-1S semi-microbalance from Sartorius. GMA and DMAEMA monomer incorporations were quantified from Fourier-transform infrared (FTIR) analysis measured on a Nicolet iS20 spectrometer. About 10 mg of dry NGs were used to measure in ATR mode. Fityk software was used to treat the data and achieve peak deconvolution. The consumption kinetics of dPG, NIPAM, and NIPMAM in the synthesis of C-NG were evaluated by proton nuclear magnetic resonance (^{1}H NMR) (Figure S4). During C-NG synthesis, 0.5 mL was extracted at 5, 15, 30, 60, 120, 180, 240, and 360 min and the polymerization was quenched using 50 μL of hydroquinone. 50 μL of D_2O was added to 450 μL of the quenched solution, and the NMR spectra were collected using a Bruker AVANCE 300 spectrometer using watergate suppress NMR mode. NMR of dry NGs were measured by dissolving about 15 mg of samples in 500 μL of D_2O. Nuclear Overhauser effect spectroscopy (NOESY) NMR spectra were acquired using a Bruker 500 MHz spectrophotometer.

The NGs' hydrodynamic diameter, surface charge, and concentration measurements were performed using a Zetasizer Ultra dynamic light scattering (DLS) device from Malvern. Particle concentration measurements were achieved by recording the averaged time for photon count-rate scattered by the sample and achieving a transformation of the size distribution using multiangle DLS (MADLS) one of inbuilt features in Zetasizer Ultra. Samples were prepared at a concentration of C = 1 mg/mL and measured in water for size measurements and in 10 mM KCl salt solution (for zeta potential measurements) using the 174.7° backscattering configuration. The values presented for hydrodynamic diameters correspond to z-average values obtained directly from zetasizer software by deconvolution of the measured correlogram, using a non-negative least-squares (NNLS) fitting algorithm. The fluctuations in scattered light intensity caused by Brownian motion were captured, and its autocorrelation is related to the diffusion coefficient. Finally, the hydrodynamic diameter was calculated from the Stokes−Einstein equation. Each set of NGs was synthesized twice, and the deviations in size, PDI, and zeta potential were determined based on triplicate measurements of these duplicated NGs. Titrations were performed with an MPT-3 autotitrator, using approximately 15 mL of a 1 mg/mL solution of NGs. Titrations were carried out using hydrochloric acid (0.25 M), sodium hydroxide (0.25 M) and acetic acid (0.025 M) as respective strong acid, strong base, and weak acid.

Cryo-SEM measurements were performed using a JEOL 7001F scanning electron microscope equipped with a PP3000T Cryo System manufactured by Quorum Technologies. The PP3000T Cryo System utilizes the nitrogen slush plunge-freezing method for rapid sample freezing. Liquid nitrogen freezes at 63 K (−210 °C) over a wide range of pressure values. Plunging an object into slushed nitrogen results in more rapid cooling than plunging into liquid nitrogen at its boiling point (−196 °C). The measurements were performed following the manufacturer's protocol PP3000T User Manual v.1.4. For the measurements, approximately 30 μL of a C = 1 mg/mL NGs solution was used. Following freezing, the specimen was transferred to the column-mounted preparation chamber, where it was fractured, sublimated (−90 °C, 60 min), and sputtered by Pt target. The observation was performed at $-190^{+}/-2$ °C (vacuum level ≈ 2.6×10^{-5} Pa), and secondary electron images were acquired at 5 keV.

Transmission electron microscopy (TEM) measurements were carried out on a JEOL JEM-1400PLUS (40 kV-120 kV) TEM. The samples were prepared using carbon grids. The grids were first plasma cleaned before the addition of 1 μL of a 0.05 mg/mL sample solution; 2 μL of a saturated ammonium molybdate solution was used as a stainer. The excess of water was absorbed with a paper, and the grids were dried for 10 min. The micrographs are reported without further image treatment. Size histograms were plotted from the TEM micrographs by using ImageJ software.

Atomic force microscopy (AFM) measurements were conducted with a VEECO (Bruker) Multimode V AFM using the conventional tapping mode. Samples were prepared by dropping 1 μL of a 0.05 mg/mL sample solution on a mica sheet and measuring using RTESP 150 (Bruker) tips. Images were treated by NanoScope software (flattening and scale bar adjustments). First, the effect of the hardness of the tip on the measurement was tested using tips with three different spring constants: 0.35 (SNL 10), 5 (RTESP 150), and 37 N/m (TESP V2). DMAEMA B-NG 20, GMA B-NG 20, GMA SB-NG 20, and ED-GMA SB-NG 20 were measured with each tip, and the hardness of the tip was observed to have a significant effect on the height and phase micrographs. The height measured was reduced from those of RTESP 150 and TESP V2. A hard tip can deform the soft NGs by spreading them on the substrate during the measurement. Second, the contrast of the height and phase micrographs increases with the hardness of the tip. RTESP 150 tips were selected as a compromise on this contrast, and then the tapping conditions were optimized. Soft tapping (amplitude set point > 15 nm) did not allow enough contrast in the micrographs. Moderate tapping (amplitude set point ≈ 10 mV) and hard tapping (amplitude set point ≈ 5 mV) were compared, and the optimized conditions were found for an amplitude set point of about 10 nm, with a drive amplitude of about 2000 mV and a drive frequency of about 120 kHz.

Small angle X-ray scattering (SAXS) experiments were carried out at the Austrian SAXS beamline at the Elettra Synchrotron, Trieste, Italy. Measurements were performed at 20 °C in the μDrop, an automatic sample changer system developed in the beamline.[33] The μDrop system is configured to measure a very low amount of sample, which is dispensed between two rectangular windows, each one consisting of a 3 mm × 1 mm-large observation area made of 2 μm-thick silicon nitride, supported by a 1 mm-wide silicon frame. The rate

https://doi.org/10.1021/acs.macromol.4c00350
Macromolecules 2024, 57, 6035−6048

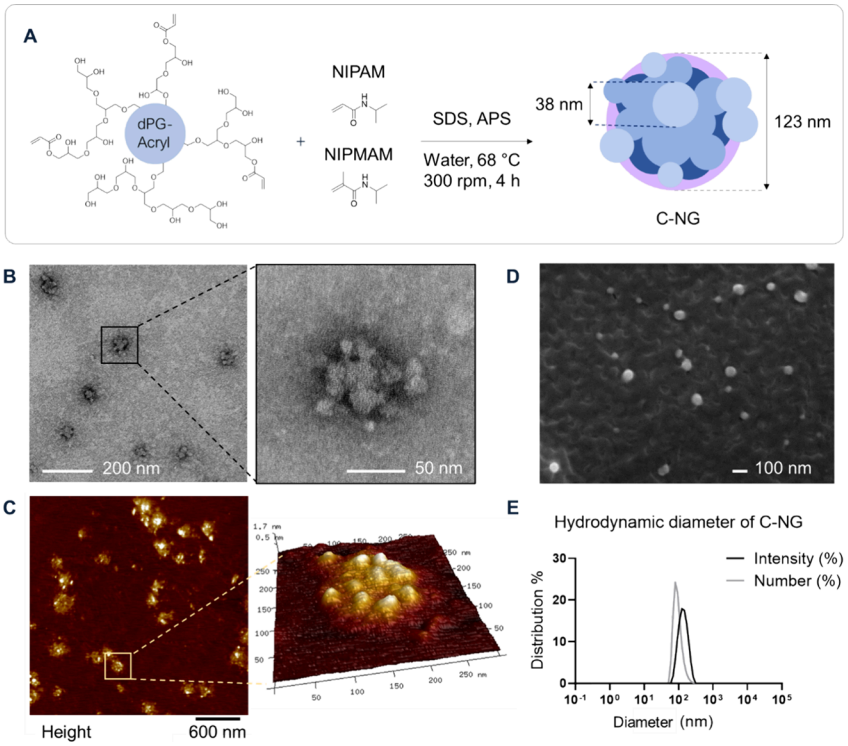

Figure 1. (A) Synthesis scheme of C-NG with the resulting NG morphology. Sizes displayed on the scheme result from DLS (hydrodynamic diameter) and SAXS measurements (subunit size) carried out in water. (B) TEM of C-NGs with a zoomed-in section (right micrograph). (C) AFM of C-NGs with zoomed section in 3D (right micrograph). (D) Cryo-SEM of C-NGs. (E) Hydrodynamic diameter of C-NGs measured by DLS.

of successful drop placement was optimized with test measurements before the experiment. At least three different injections for each sample were performed to obtain triplicate measurements. Each SAXS acquisition lasted for 10 s, with a rest time of 3 s for each step, and for each sample injection, 18 acquisitions were obtained. Rest time reduces the possibility of radiation damage. Samples and buffers were measured under the same temperature and exposure time conditions. Incident and transmitted beam intensities were measured to obtain the transmission values. The two-dimensional patterns were recorded with the Pilatus3 1 M detector system (Dectris, Switzerland), processed by SAS DOG[34] and by Igor Pro software (WaveMetrics, Lake Oswego, OR, USA) to obtain radial averages. The scattering intensity, expressed as macroscopic differential scattering cross section $d\Sigma/d\Omega$, was obtained as a function of the magnitude of the scattering vector Q, defined as $Q = 4\pi \sin \theta/\lambda$, where 2θ is the scattering angle, and $\lambda = 0.154$ nm is the wavelength of X-rays corresponding to an energy of 8 keV. The sample−detector distance was 1.558 m. The maximum Q was 3.5 nm^{-1}. C-NGs in water were measured as a function of time, with 4 h as the end point at a concentration equal to 1 mg/mL.

SAXS data were analyzed by Beaucage model of polymeric mass fractal.[35] The main resulting parameters are R_g, the radius of gyration whose value should correspond to the overall dimension of the species in solution, R_{sub}, the substructural gyration radius, and P, which describes the fractal behavior of the samples. When P parameter is between 3 and 4 the model describes a surface fractal. Values of P lower than 3 indicate a mass fractal, while P values greater than 4 indicate a diffuse interface. Data analysis was performed using GENFIT software.[36] The equation used in the model and the SAXS curve fittings is reported in the SI (Figure S5).

2,4,6-Trinitrobenzenesulfonic acid (TNBSA) assays were performed for the quantification of the primary amines in the EDGMA SB-NG. 200 μL of a NG solution (2 mg/mL) in Na_2CO_3 buffer (pH 9.5) were mixed with 50 μL of TNBSA solution (0.1%) in 96-well plate and kept for 2 h at 37 °C. After 2 h, absorbance was measured at 420 nm with a Biotek Synergy Neo2 plate reader.

The NGs' VPTTs were measured by differential scanning calorimetry (DSC) using a Microcalvet microcalorimeter from Setaram. 300 μL of C = 5 mg/mL sample solutions were measured from 20 to 70 °C with heating and cooling rates of 0.5 °C/min, using water as a reference.

RESULTS AND DISCUSSIONS

Batch Copolymerization of dPG-Acryl, NIPAM, and NIPMAM. The synthesis strategy employed in this work aimed to develop core−shell NGs with a positively charged core. It was initially hypothesized that by manipulating the disparity in hydrophobicity between the monomers, core−shell NGs could be obtained by precipitation polymerization. Hydrophobic monomers (such as GMA) were expected to promote precipitation and condense within the core, while the more hydrophilic NIPAM/NIPMAM units would act as stabilizers and be placed on the surface. Therefore, GMA-NIPAM/NIPMAM core−shell structures could be obtained through a one-step precipitation reaction driven by hydrophobic interactions. Subsequently, the functionalization of GMA via the epoxy ring by the amine group (ED) would finally lead to core−shell NGs with positively charged cores.

In the first step, C-NGs were synthesized (Figure 1A) and the precipitation mechanism was investigated. The NG morphology was characterized in dry condition by TEM and AFM (Figure 1B,C), and in swollen state by cryo-SEM (Figure 1D). TEM and AFM evidenced raspberry-like structures in the dry state. The NGs appeared as multiglobular structures formed by the agglomeration of smaller subunits. Interestingly, these subunits were no longer visible in cryo-SEM micrographs, where the NGs displayed a spherical morphology. In such conditions, the subunits were probably hidden within the

https://doi.org/10.1021/acs.macromol.4c00350
Macromolecules 2024, 57, 6035−6048

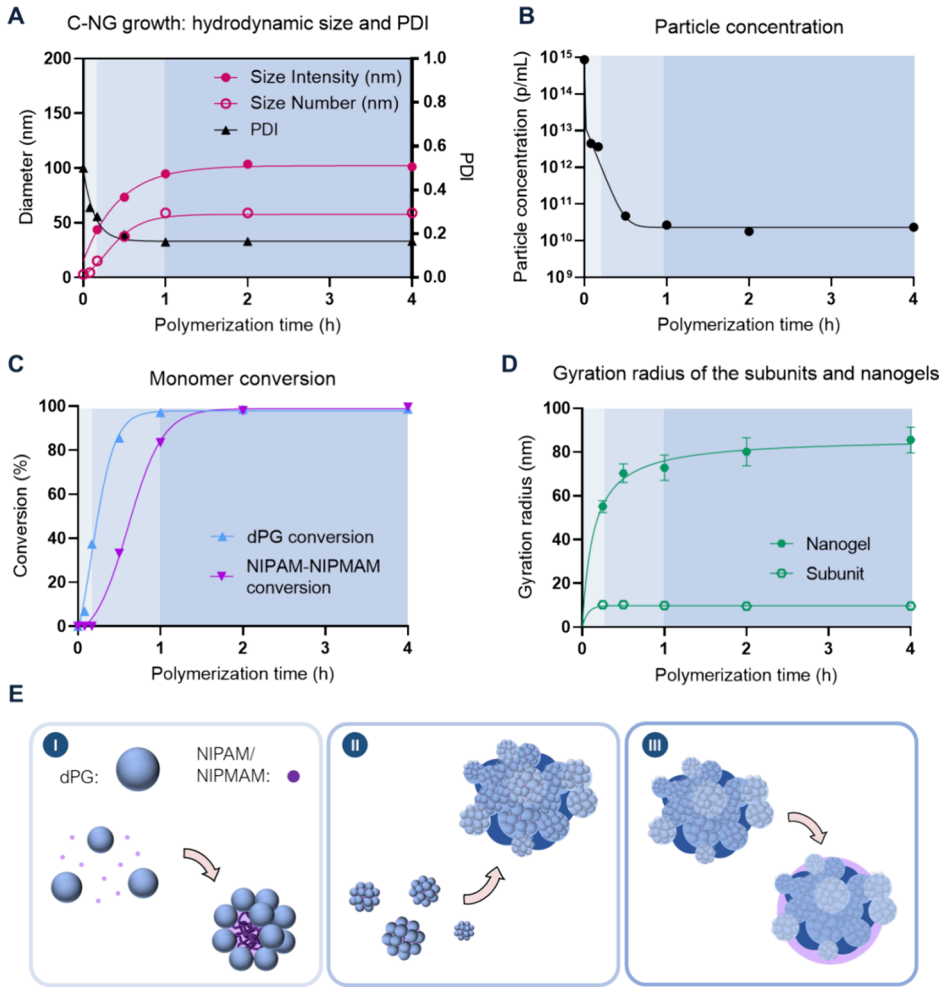

Figure 2. C-NG growth kinetics and proposed mechanism of NG formation. (A) Size and PDI during C-NG synthesis measured by DLS. (B) Particle concentration determined by MADLS. (C) Monomer conversion determined by NMR. Here NIPAM and NIPMAM have a similar conversion profile compared with dPG and are plotted together. (D) Gyration radius of the subunits and of the overall structure of NGs calculated from SAXS and obtained from Beaucage fractal model. (E) Hypothesized mechanism of the raspberry-like NG formation via (I) formation of nuclei, (II) precipitation and cross-linking of the nuclei, and (III) maturation of the NGs. These three phases are represented in (A–D) by the three corresponding shades of blue.

structure or fully stretched due to the swelling of the polymeric structure in aqueous conditions.

The z-average hydrodynamic diameter (D_H) of the NGs determined by DLS was about 100–120 nm by number and intensity distributions, as shown in Figure 1E. The similar values obtained for the number and intensity distribution indicate a low polydispersity of the particles in water. The average diameter of the NGs was also measured in dry state from TEM and AFM micrographs, with respective values of 74 ± 16 and 181 ± 50 nm (Figures S6–S8). Smaller diameters were obtained by TEM in comparison with AFM due to artifacts inherent to the measurement method. Some artifacts could result from the TEM sample preparation using ammonium molybdate as contrast agent. In this staining method, the contrast agent could penetrate the less dense outer region of the NG during sample preparation, making it invisible on the micrographs. In opposition, AFM could capture the whole structure, but in this case the force applied by the tip in conventional tapping mode could promote some spreading of the NG on the surface.[37] The subunits in both TEM and AFM micrographs displayed a large size dispersion between ∼10 to ∼40 nm. Besides the subunit size heterogeneity observed in dry state, the number of subunits within each NG seemed to vary from one NG to another, indicating a nonhomogeneous growth of the NGs.

The hydrophilicity of the cross-linker in the precipitation polymerization greatly impacts the formation of the structure. It has been reported that hydrophilic macro-cross-linkers could stabilize small precipitating nuclei during polymerization.[29,38] To investigate more in depth the role of dPG in precipitation polymerization, the kinetics of monomer conversion were determined by ^{1}H NMR (Figure S4) and compared with the NG growth rate and particle concentration during the synthesis. It is shown in Figure 2 that the final size (Figure 2A) and concentration (Figure 2B) of the NG reached a plateau after 1 h of reaction, after full consumption of dPG (Figure 2C). During the cross-linker conversion, the NG size increases rapidly to almost reach its final size while the particle concentration drops exponentially. This rapid drop in particle number together with the nanoparticle growth during the first hour suggests the combination of many small nanoparticles to form the final NG particles. Then, a maturation phase occurs in the second hour of polymerization, where NIPAM and

https://doi.org/10.1021/acs.macromol.4c00350
Macromolecules 2024, 57, 6035–6048

Table 1. Summary of the Mass Yield, Hydrodynamic Diameter (D_H), PDI, and Zeta Potential of NGs, and DMAEMA and GMA Mass Concentrations

sample	mass yield (%)	D_H (nm)	PDI	zeta potential (mV)	DMAEMA or GMA concentration (% wt)
C-NG	91.3 ± 0.5	123 ± 2	0.115 ± 0.005	−1.1 ± 0.1	
DMAEMA B-NG 5	91.0 ± 0.5	165 ± 14	0.134 ± 0.048	+4.4 ± 1.7	2.6 ± 0.9
DMAEMA B-NG 10	81.6 ± 2.3	167 ± 13	0.227 ± 0.144	+8.0 ± 0.8	8.1 ± 3.3
DMAEMA B-NG 20	70.3 ± 0.5	157 ± 8	0.104 ± 0.010	+11.0 ± 0.8	21.3 ± 3.3
DMAEMA SB-NG 5	29.8 ± 0.5	159 ± 105	0.321 ± 0.000	+7.1 ± 3.1	63,4 ± 8.0
DMAEMA SB-NG 10	31.7 ± 1.0	42 ± 1	0.552 ± 0.219	+9.2 ± 3.2	78.7 ± 5.7
DMAEMA SB-NG 20	37.6 ± 1.0	40 ± 1	0.567 ± 0.145	+16.2 ± 3.9	105.9 ± 5.2
GMA B-NG 5	96.8 ± 1.6	152 ± 4	0.066 ± 0.013	−0.8 ± 0.2	8.5 ± 2.9
GMA B-NG 10	95.7 ± 0.0	158 ± 18	0.063 ± 0.004	−1.3 ± 0.3	12.1 ± 1.6
GMA B-NG 20	95.0 ± 2.1	407 ± 277	0.594 ± 0.575	−1.3 ± 0.1	26.3 ± 2.3
GMA SB-NG 5	88.4 ± 4.2	149 ± 2	0.133 ± 0.002	−0.7 ± 0.2	3.6 ± 0.1
GMA SB-NG 10	82.5 ± 2.1	105 ± 3	0.143 ± 0.012	−0.9 ± 1.2	10.8 ± 0.0
GMA SB-NG 20	61.9 ± 6.2	138 ± 2	0.047 ± 0.022	−1.4 ± 0.3	18.3 ± 0.4
ED-GMA B-NG 5		144 ± 1	0.073 ± 0.083	−1.2 ± 0.0	
ED-GMA B-NG 10		137 ± 9	0.062 ± 0.004	+5.6 ± 0.4	
ED-GMA B-NG 20		298 ± 69	0.163 ± 0.139	−1.2 ± 0.2	
ED-GMA SB-NG 5		156 ± 0	0.128 ± 0.015	−0.4 ± 0.3	
ED-GMA SB-NG 10		110 ± 5	0.160 ± 0.031	−0.8 ± 0.9	
ED-GMA SB-NG 20		142 ± 3	0.069 ± 0.020	−0.1 ± 1.8	

NIPMAM almost reach complete conversion, resulting in a slight size increase of the raspberry-like NGs.

Besides NMR and DLS kinetics, SAXS experiments were performed in order to obtain complementary structural characterization. SAXS curves analysis has been performed according to Beaucage fractal model aiming to describe the size of the aggregates and of the subunits during the NG growth.[35] The gyration radii of the whole NGs (R_g), reported in Figure 2D, increase from ∼55 to ∼90 nm with increasing polymerization times from 15 min to 4 h. This trend is in agreement with DLS results (Figure 2A), considering the differences between the two scattering techniques, in terms of radiation wavelengths and of theoretical approximation due to polydisperse objects. On the other hand, substructure radius R_{sub} during the kinetic process maintains around a value of 10 ± 2 nm. This fact hints that polymerization proceeds via subunit association and produces structures resembling fractals. In fact, the fractal exponent value moves from a surface fractal to a mass fractal at increasing times (Figure S5B).

Thus, the kinetics study revealed an agglomeration mechanism where small nanoparticles stabilized with dPG grow, precipitate and cross-link, as schematized in Figure 2E. In this hypothesis, precipitation is driven by the growth of the P(NIPAM)-*co*-P(NIPMAM) chains. In the first phase, the nuclei are obtained from the stabilization of small P(NIPAM)-*co*-P(NIPMAM) chains by dPG. Then, while P(NIPAM)-*co*-P(NIPMAM) chains keep growing, the nuclei's stability decreases until precipitation. In this second phase, the precipitates cross-link until the full consumption of dPG. In the last phase, the remaining NIPAM and NIPMAM monomers finish polymerizing within the stabilized cross-linked structures. Here, the mechanism only involves a one-step synthesis, in opposition to most of the polymeric systems yielding raspberry-like nanoparticles usually based on the cross-linking of presynthesized nanoparticles or on the heterogeneous growth of polymers using a template.[39,40]

While some research groups already worked on the synthesis of core−shell NGs using precipitation polymerization, all the examples are based on low molecular weight cross-linkers.[23,24] In our study, we distinguish our approach by employing dPG as a cross-linker. Whereas NGs are expected to grow homogeneously with low molecular weight cross-linkers, dPG stabilizes some small nanoparticles and triggers the heterogeneous precipitation via the formation and binding of the small subunits. The homogeneous growth results in the simplest spherical morphology, whereas heterogeneous growth might provide more complex structures, such as these raspberry-like nanoparticles. This growth mechanism is also likely to provide different mechanical properties and swelling behavior from NGs growing homogeneously, in which case the cross-linker incorporation can directly be related to the radial density of polymers.[41]

It was already anticipated that due to this growth mechanism by binding smaller NG seeds, preparing a perfect core−shell structure would be challenging by simple batch copolymerization.

Batch Copolymerization of DMAEMA or GMA. Aiming to introduce positive charges into the dPG-NIPAM-NIPMAM NGs, two different monomers were considered: DMAEMA and GMA. DMAEMA is a water-soluble monomer displaying a tertiary amine. P(DMAEMA) shows high transfection abilities and has been used for gene delivery for more than two decades.[42,43] Due to its high hydrophilicity and ideal copolymerization behavior with NIPAM, the batch copolymerization of DMAEMA with NIPAM and NIPMAM was not expected to result in phase segregation within the NG structure.[27,44,45] For this reason, DMAEMA B-NG served as a control for NG without a core−shell structure. On the other hand, GMA is relatively hydrophobic and was expected to migrate to the NG core during the polymerization in water. Moreover, GMA has been reported to polymerize faster than NIPAM in an ideal copolymerization.[46] Its higher reactivity promotes phase separation in the NG by promoting block copolymerization. In addition, GMA is a reactive monomer that can be used as a "plug and play" tool to introduce positive charges from different nature.[47] Here, amine functionalization

https://doi.org/10.1021/acs.macromol.4c00350
Macromolecules 2024, 57, 6035−6048

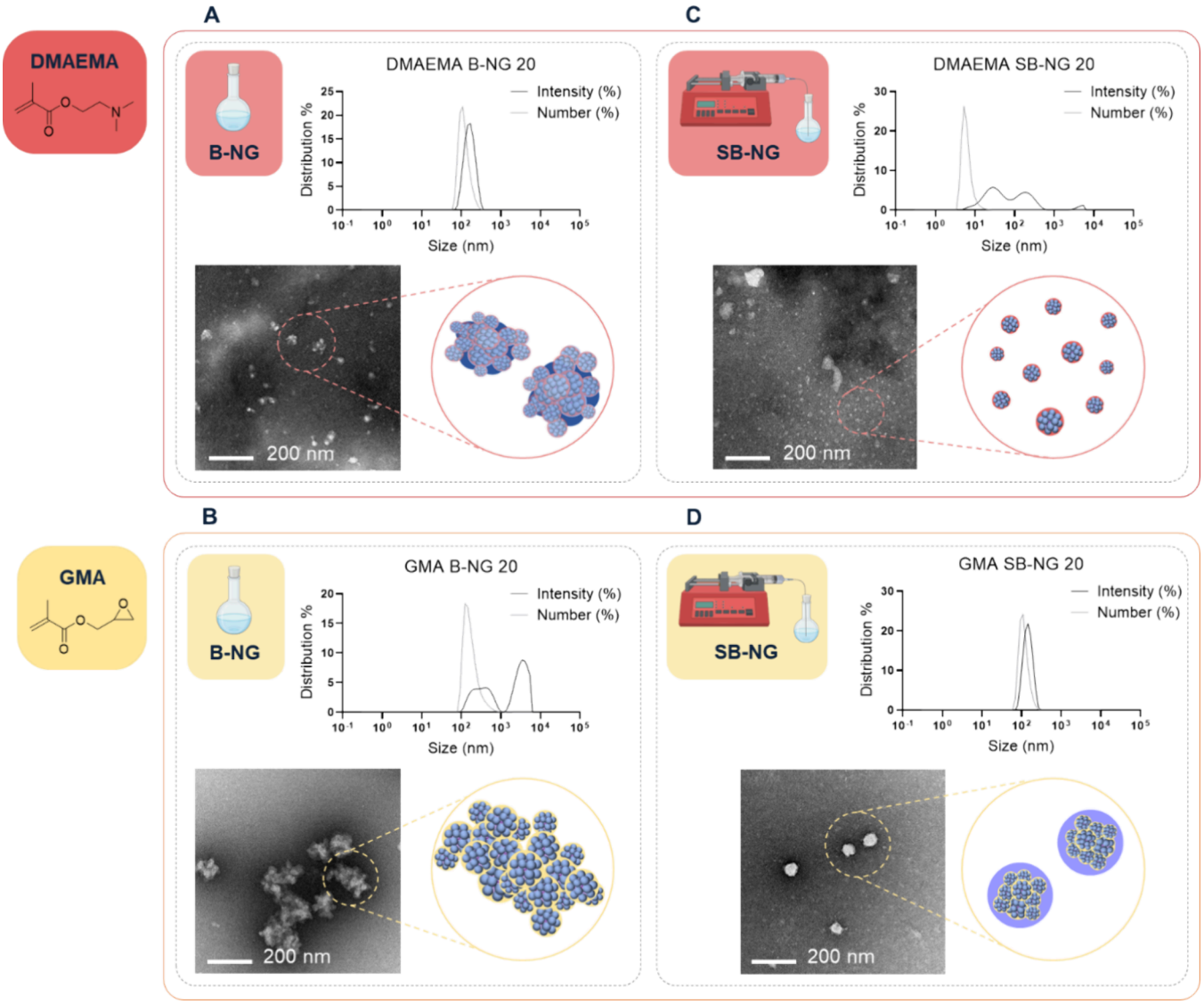

Figure 3. Representative of hydrodynamic diameter obtained by DLS, the morphology observed by TEM, and a schematic depiction of (A) DMAEMA B-NG 20, (B) GMA B-NG 20, (C) DMAEMA SB-NG 20, and (D) GMA SB-NG 20.

was carried out via the GMA epoxy group through nucleophilic addition and ring opening using ED.

The copolymerization of DMAEMA with the other monomers at 5, 10, and 20% w/w via precipitation polymerization yielded the production of positively charged NGs of about 160 nm and a relatively low polydispersity (PDI), as shown in Table 1. As the concentration of DMAEMA increases in the NG, the total mass yield decreases from more than 90 to 70% for the highest concentration. This reduction is caused by the increase in the hydrophilicity of the NGs and indicates a reduction in the precipitation yield. The hydrodynamic diameter increase of the charged systems is likely due to the inner electrostatic repulsions and higher degree of hydration (Table 1). MADLS was also performed at three distinct detection angles: back scatter (174.7°), side scatter (90°), and forward scatter (12.78°) for obtaining the angular dependence on hydrodynamic diameter (Table S3).

In contrast to DMAEMA, the copolymerization of GMA reaches a higher yield than that of C-NGs. As expected, more hydrophobic monomers promote precipitation. Hydrodynamic diameter of about 150 nm were obtained for the lower concentrations, and negative zeta potential was measured due to the surface exposition of the initiator.[48] For both DMAEMA and GMA B-NG 20, TEM micrographs still show raspberry-like NGs (Figure 3A,B). On the micrographs, the PDI of GMA B-NG 20 seems wider than that of DMAEMA B-NG 20 as confirmed by DLS, indicating the limit in GMA B-NG 20s stability (Table 1). The size distribution of the NGs is also reflected by the difference in the hydrodynamic diameters expressed by intensity and number, measured by DLS (Figure S4). As expected, the hydrodynamic diameters expressed by number are smaller than the ones by intensity: in the size distribution by intensity, larger particles contribute disproportionately more than small particles, whereas this weighting in the size distribution does not depend on the size in the number-based distribution.

Cryo-SEM measurements indicate spherical morphologies for DMAEMA B-NG 20 in the swollen state, whereas GMA B-NG 20 appears as irregular NGs with a large dispersity (Figure S9). These observations confirm the low control in the stabilization of the GMA B-NGs during the precipitation due to their excessive hydrophobicity. After lyophilization,

https://doi.org/10.1021/acs.macromol.4c00350
Macromolecules 2024, 57, 6035−6048

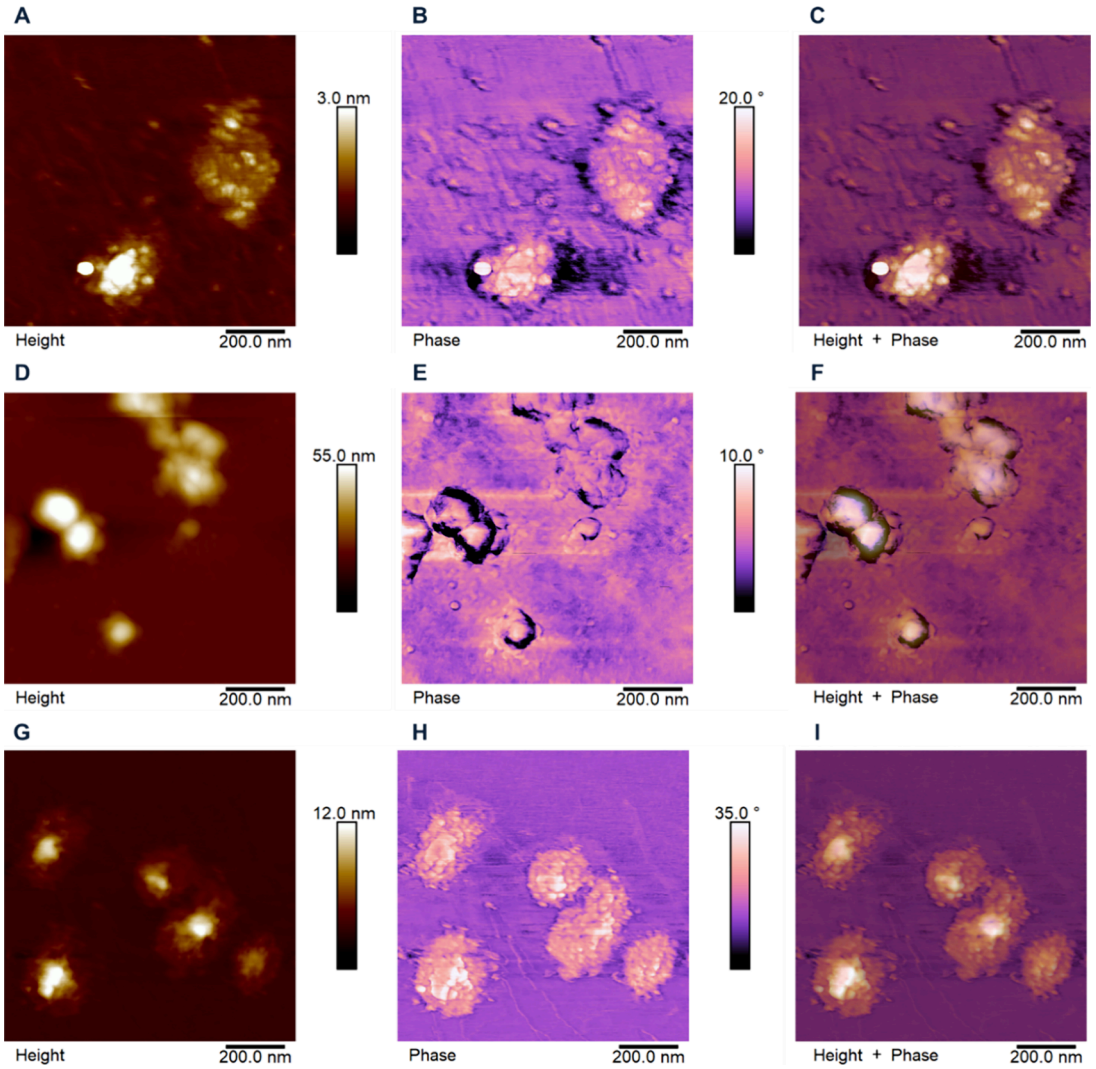

Figure 4. AFM height, phase, and superposition of height and phase imaging of DMAEMA B-NG 20 (A–C), GMA B-NG 20 (D–F), and GMA SB-NG 20 (G–I).

aggregates were observed for GMA B-NG 20, shown by their large sizes and PDI values measured by DLS (Tables S4 and S5). This observation is likely due to the presence of hydrophobic points on the surface of the NGs, and the absence of P(NIPAM)-*co*-P(NIPMAM) shell. It is important to remember the proposed mechanism in which raspberry structures were obtained (Figure 2C). Even if some nuclei mainly composed of GMA would migrate to the core of the NGs, perfect core–shell structures would be difficult to obtain, as the growth occurs by fusion and not merely nuclei growth.

DMAEMA and GMA incorporation were evaluated by FTIR.[49,50] The introduction of the methacrylate monomers results in an increase in the 1725 cm^{-1} ester peak, which can be quantified by deconvolution (Figures S10–S13). Good incorporation of the monomers was shown for both DMAEMA B-NGs and GMA B-NGs with slightly higher GMA concentrations than DMAEMA (Table 1, Figure S14).

Semibatch Copolymerization of DMAEMA or GMA. Aiming to improve the core–shell feature of the NGs, semibatch copolymerizations were carried out. Several groups worked on core–shell structures via a two-step precipitation polymerization where the nuclei are first synthesized, before the shell addition in a postprecipitation reaction.[22–24] In this work, the core–shell structure was aimed at in a one-step synthesis. NIPAM and NIPMAM were added over 1 h from the start of the reaction. Since GMA has been reported to have a higher reactivity than NIPAM, one could assume that the semibatch reaction conditions would enhance the monomer separation in the final polymers.[46] Then, the phase separation due to hydrophobic segregation would be enhanced.

For the DMAEMA SB-NGs, the initial solution contained only dPG and DMAEMA as monomers. Due to their high hydrophilicity, they did not precipitate into NGs as DMAEMA B-NGs, as shown by DLS (Figure 3C). Only small nanoparticles were obtained, corresponding to the subunit's sizes described previously. Their high dispersity revealed by DLS and TEM implies a low control during the precipitation. The DMAEMA concentration calculated from FTIR measurements indicate low incorporation of NIPAM and NIPMAM (Table 1, Figure S14). Therefore, the early stabilization of small DMAEMA-dPG nanoparticles prevents the copolymerization and incorporation of NIPAM and NIPMAM, which are cleared during purification.

In contrast to DMAEMA, GMA SB-NG were successfully synthesized, yielding NGs with a low polydispersity index of <0.16. Here, the polymerization of GMA promoted the

https://doi.org/10.1021/acs.macromol.4c00350
Macromolecules 2024, 57, 6035–6048

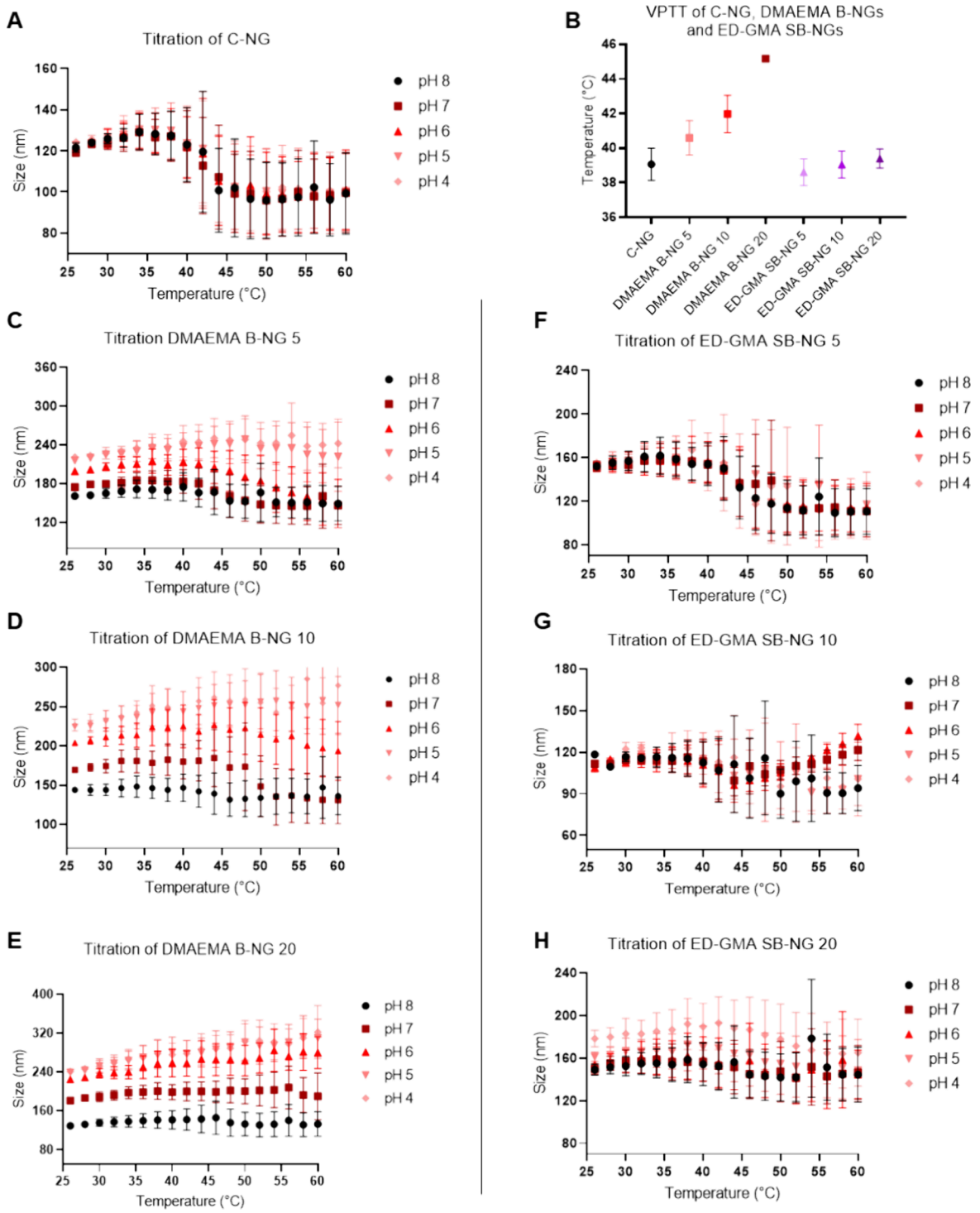

Figure 5. (A) Temperature and pH responsiveness of C-NG characterized by DLS. (B) VPTT of C-NG, DMAEMA B-NG 5, 10, 20, and ED-GMA SB-NG 5, 10, and 20 measured by DSC. The error bar originates from the measurement of the heating and the cooling ramp. Temperature and pH responsiveness of (C) DMAEMA B-NG 5, (D) DMAEMA B-NG 10, (E) DMAEMA B-NG 20, (F) ED-GMA SB-NG 5, (G) ED-GMA SB-NG 10, and (H) ED-GMA SB-NG 20 characterized by DLS. The DLS titrations show the hydrodynamic diameter of the NGs from 26 to 60 °C, from pH 8 to 4.

precipitation and allowed the successful copolymerization with NIPAM and NIPMAM. The good solubility and stability of GMA SB-NG 20 compared with GMA B-NG 20 suggests the enhancement of the surface hydrophilicity by the semibatch method. This is further supported by TEM micrographs: the NG surface looks smoother for SB-NGs, and the subunits are not as visible as those for B-NGs (Figure 3D). This could be due to the formation of a P(NIPAM)-*co*-P(NIPMAM) coating by homogeneous growth after the formation of the raspberry-like GMA-dPG nuclei.

AFM was measured in tapping mode, and height and phase contrast images were collected (Figures S17 and S18). In phase contrast imaging, the phase shift of the cantilever is displayed; this shift is impacted by the softness, adhesion,

https://doi.org/10.1021/acs.macromol.4c00350
Macromolecules 2024, 57, 6035−6048

viscoelasticity, and roughness of the surface measured, and also depends on the tapping hardness.[51] Therefore, this imaging mode unveils the Supporting Information to the height mode, where only the material thickness can be observed.[52] There, high resolution of the NG edges can be obtained since the NGs are much softer than the mica substrate. To combine both information collected from the height and phase imaging, both micrographs were superposed for DMAEMA B-NG 20, GMA B-NG 20, and GMA SB-NG 20 and are displayed in Figure 4. On these superpositions, the inner organization is clearly seen, with a precise imaging of both the NG dense points and edges. While DMAEMA B-NG 20 looks very soft (Figure 4A−C), GMA B-NG 20 seems denser and does not spread on the substrate (Figure 4D−F). In opposition to both, GMA SB-NG 20 micrographs clearly indicate the presence of a core−shell structure, with a denser core and softer shell, as hypothesized before (Figure 4G−I).

Small heights have been measured in AFM compared with the results found in the literature.[53−55] These observations could come from the deformation of the NGs and penetration of the tip in the polymeric network under these specific moderate tapping conditions. The height of C-NGs in the dry state was around 2 nm, whereas its diameter was about 180 nm. These values should be considered only in the context of the moderate tapping mode: the NGs are likely to spread on the surface. The maximum heights are observed in the subunits where the cross-linker are probably highly concentrated. It is likely that the raspberry organization endows high flexibility to the structure. While DMAEMA NGs still showed heights of a few nanometers, GMA NGs are characterized by higher heights (about 10 to 50 nm). This might be due to the reactivity and hydrophobicity of GMA. Compared with DMAEMA NGs, the subunits with GMA might precipitate quicker due to their higher hydrophobicity. Therefore, they might have higher cross-linking point in between the subunits, making the whole structure more rigid.

Regarding the core−shell NGs, a high concentration of cross-linker (dPG) was expected in the core, whereas the shell was made principally of NIPAM and NIPMAM via the slow addition and after the consumption of GMA and dPG. AFM was able to confirm these results by the characterization. Still, the diameter and height of the NGs provided by AFM should only be considered in the context of the moderate tapping conditions in the dry state. In these conditions, the shell seems to spread and adopt a "fried egg" structure, as previously reported.[56]

GMA Functionalization. The reaction conditions of GMA-B NGs functionalization with ED were set with high temperature, long reaction time, and high ED equivalents to limit the internal cross-link points. Indeed, besides ED two nucleophilic ends, it is known that primary amine groups could react several times with epoxy groups.[47] Figures S20 and S21 illustrate FTIR and NMR spectra, which provide evidence of GMA ring opening through ED functionalization. TNBSA assays confirmed the presence of primary amines in GMA SB-NG, with low reaction yields (Figure S22). After functionalization, the surface charge changed from negative to positive for all of the GMA SB-NGs at 50 °C, proving the incorporation of the amine groups (Figure S23). The AFM micrographs revealed the vanishing of the core−shell characteristic after functionalization, plausibly attributed to the apparent diminution in the hydrophobicity of the core due to the charge incorporation (Figure S26). The amine incorporation evidenced by spectroscopy, together with the structural change of the NGs' core observed by microscopy, confirmed the preferential accumulation of the amines in the core of ED-GMA SB-NGs.

pH and Thermoresponsiveness. Herein, we studied the dual responsiveness of DMAEMA B-NGs and ED-GMA SB-NGs. DMAEMA B-NGs were selected for their homogeneous distribution of the amine groups in the structure and used for comparison with ED-GMA SB-NGs. The presence of primary to tertiary amines that can protonate at pH under the pK_a, makes both systems pH-sensitive, while the P(NIPAM)-*co*-P(NIPMAM) segments bring thermoresponsive behavior.

The VPTT of NGs was assessed through DSC (all DSC scans appear on Figure S27) and DLS over a temperature range of 25−60 °C. First, the C-NGs present a sharp VPTT around 39 °C, independent of the pH, as demonstrated by DLS and DSC and in accordance with other reports (Figure 5A,B).[31] At this transition and with an increase in the temperature, the interaction between water and the P(NIPAM)-*co*-P(NIPMAM) segments is disrupted to favor intermolecular bonding of the polymeric chains, resulting in the collapse of the structure and in the reduction in size about 30 nm. The incorporation of DMAEMA in the NGs results in a clear increase in the VPTT, as demonstrated by DSC (Figure 5B). In agreement with previous reports, the transition temperature increases from 39 to 45 °C for DMAEMA B-NG 20.[44] The elevation in the VPTT of the NGs can be attributed to the incorporation of the hydrophilic repeat unit in the cross-linked copolymers. Indeed, the introduction of positive charges favors the hydration of the NGs over intermolecular hydrogen bonding of P(NIPAM) and P(NIPMAM) chains crucial for water expulsion and the subsequent collapse of the NGs.[57,58] In other words, the hydration of tertiary amines increases the hydrophilicity of the NGs and prevents their collapse. This increase in the VPTT indicates that the NGs require more energy to disrupt hydrogen bonding with water and to form intramolecular interactions.

The titration of DMAEMA B-NG 5, 10, and 20 using DLS at different temperatures demonstrated that the hydrodynamic diameter of the NGs depends on the pH and increases with a reduction of pH from 8 to 4 (Figure 5C−E). Although a VPTT is still observed for DMAEMA B-NG 5 at pH 8 to 6, the size reduction effect of this transition seems to disappear for the rest of the NGs with higher DMAEMA concentrations at all pHs. At low pH, the hydrodynamic diameter even seems to increase with increasing temperatures, as observed for DMAEMA B-NG 20 (Figure 5E). For the most charged NGs, the presence of the hydrophilic to hydrophobic phase transition along with the increase in the hydrodynamic diameters of the NGs seems contradictory. The intramolecular hydrogen bonding between P(NIPAM)-*co*-P(NIPMAM) must occur to expel the water and trigger the NGs' collapse. Yet, in the hydrated state of the NG due to the random copolymerization of the amine-containing monomer in the NGs, the energy gain of the intramolecular hydrogen bonding and entropy increase due to the release of hydration water are probably not enough to compensate for the loss of enthalpy that would imply the dehydration of the amines. In this hypothesis, the presence of tertiary amines favors the hydrated state over the intramolecular interactions, explaining the increase in the hydrodynamic diameter even when P-

https://doi.org/10.1021/acs.macromol.4c00350
Macromolecules 2024, 57, 6035−6048

(NIPAM)-*co*-P(NIPMAM) polymers are in the hydrophobic state.[59]

For ED-GMA SB-NGs, a slight increase in VPTT was observed (Figure 5B). This small change compared with DMAEMA B-NGs could be explained by the low ED incorporation and the phase separation: as NIPAM and NIPMAM were added in a semibatch method and due to GMA high reactivity, the shell is mainly composed of P(NIPAM)-*co*-P(NIPMAM). Therefore, the VPTT is not affected as much as for DMAEMA B-NGs where DMAEMA is likely to be randomly copolymerized within the entire structure. Again, the introduction of the primary and secondary amines in the NGs affects their thermoresponsive behavior (Figure 5F−H). The reduction in the hydrodynamic diameter due to the NG collapse above the transition temperature was not observed for ED-GMA SB-NG 20.

Zeta potentials of the NGs were measured at temperatures below and above the VPTT and are displayed in Figure 6. As

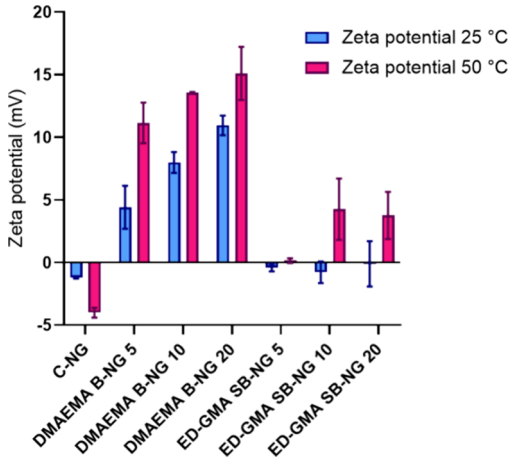

Figure 6. Thermoresponsiveness of DMAEMA B-NGs and ED-GMA SB-NGs observed through the evolution of the zeta potential at temperatures below and above the transition temperature.

observed for C-NG and DMAEMA B-NGs, when the NGs collapse above the transition temperature, the zeta potential value increases. For DMAEMA B-NGs, an increase of about 5 mV was observed. This enhancement of the surface charge is a result of a rearrangement of the structure. Probably, some P(NIPAM)-*co*-P(NIPMAM) segments collapse inward, while the charged moieties are exposed on the surface. The behavior of ED-GMA SB-NGs' zeta potential is different from DMAEMA B-NGs. From very slight negative values, practically neutral, the zeta potential grows to positive values when crossing the VPTT. Since a P(NIPAM)-*co*-P(NIPMAM) shell surrounds the positive charges, almost neutral zeta potential values are obtained below the transition temperature. When increasing the temperature above the VPTT, the shell might collapse, displaying the positive charges from the swollen core.

The data clearly show that the incorporation of amines in the NGs considerably affects their thermoresponsive character. With increasing DMAEMA or ED contents, the intensity of the phase transition caused by temperature seems to decrease due to the presence of electrostatic forces. Looking at the final application in gene delivery, this effect appears as a challenge to achieve thermocontrolled nucleic acid delivery. Despite the hydrodynamic evolution around the VPTT, the structural rearrangement suggested a possible change in the amine availability, which could be use in further gene delivery applications.

CONCLUSIONS

In this work, the mechanism of the precipitation copolymerization of dPG, NIPAM, and NIPMAM was enlightened. The dPG cross-linker was shown to stabilize small nanoparticles made of P(NIPAM)-*co*-P(NIPMAM) oligoradicals during the early growth of the NGs. Then, after the precipitation and agglomeration of the subunits, raspberry-like morphologies were obtained with a narrow size distribution. Positive charges were introduced in batch and semibatch synthesis using either direct incorporation of DMAEMA or GMA monomers with subsequent amine functionalization via epoxy ring opening. The high hydrophilicity of DMAEMA enhances the stability of the subunits and restrains precipitation, whereas the incorporation of GMA promotes precipitation. Core−shell NGs were reached by a semibatch reaction using GMA as a comonomer. DMAEMA B-NGs displayed raspberry-like structures, with a homogeneous distribution of the positive charges within the NGs. In contrast, the charges of ED-GMA SB-NGs were restricted within the core. These NGs showed unique thermal behavior, with a change from neutral to positive zeta potential when crossing the VPTT. Looking at further NG optimization for the complexation of nucleic acids and transfection, we can easily achieve a fine-tuning of the charged core by changing the amine group in the functionalization reaction. Finally, this study provides a framework for understanding the possibilities and limits of precipitation polymerization in the synthesis of NGs with advanced structures for gene delivery applications. The interaction of these NGs with biological systems is currently being investigated.

ASSOCIATED CONTENT

Supporting Information

The Supporting Information is available free of charge at https://pubs.acs.org/doi/10.1021/acs.macromol.4c00350.

Additional NMR and FTIR spectra, TEM, AFM, and cryo-SEM micrographs, SAXS, DLS, and DSC data, FTIR calibration data, and TNBSA analysis (PDF)

AUTHOR INFORMATION

Corresponding Authors

Sergio E. Moya − *Basque Research and Technology Alliance (BRTA), Center for Cooperative Research in Biomaterials (CIC biomaGUNE), Donostia-San Sebastián 20014, Spain;* orcid.org/0000-0002-7174-1960; Email: smoya@cicbiomagune.es

Marcelo Calderón − *POLYMAT, Applied Chemistry Department, Faculty of Chemistry, University of the Basque Country UPV/EHU, Donostia-San Sebastián 20018, Spain; IKERBASQUE, Basque Foundation for Science, Bilbao 48009, Spain;* orcid.org/0000-0002-2734-9742; Email: marcelo.calderonc@ehu.eus

Authors

Bruno Espuche − *Basque Research and Technology Alliance (BRTA), Center for Cooperative Research in Biomaterials (CIC biomaGUNE), Donostia-San Sebastián 20014, Spain; POLYMAT, Applied Chemistry Department, Faculty of Chemistry, University of the Basque Country UPV/EHU,*

https://doi.org/10.1021/acs.macromol.4c00350
Macromolecules 2024, 57, 6035−6048

Donostia-San Sebastián 20018, Spain; orcid.org/0000-0002-4278-9105

Krishan Kumar − *POLYMAT, Applied Chemistry Department, Faculty of Chemistry, University of the Basque Country UPV/EHU, Donostia-San Sebastián 20018, Spain;* orcid.org/0000-0002-4057-0257

Paolo Moretti − *Department of Life and Environmental Sciences, Marche Polytechnic University, Ancona 60131, Italy*

Maria Grazia Ortore − *Department of Life and Environmental Sciences, Marche Polytechnic University, Ancona 60131, Italy;* orcid.org/0000-0002-2719-6184

Olena Ivashchenko − *NanoBioMedical Centre, Adam Mickiewicz University, Poznań 61-614, Poland*

Emerson Coy − *NanoBioMedical Centre, Adam Mickiewicz University, Poznań 61-614, Poland;* orcid.org/0000-0002-4149-9720

Heinz Amenitsch − *Institute of Inorganic Chemistry, Graz University of Technology, Graz 8010, Austria;* orcid.org/0000-0002-0788-1336

Complete contact information is available at: https://pubs.acs.org/10.1021/acs.macromol.4c00350

Author Contributions

B.E. conceived and designed the research, optimized the NG synthesis, conducted DLS, Z-potential, H NMR, FTIR, TEM, AFM, and DSC experiments, analyzed data, and wrote the manuscript. K.K. contributed to experimental work performing DLS titrations and TNBSA assays, and reviewed and edited the manuscript. P.M., M.G.O., and H.A. carried out the SAXS experiments, interpreted the results, and edited the manuscript. O.I. and E.C. provide expertise in cryo-SEM characterization and edited the manuscript. SEM and M.C. supervised the project, secured funding, and critically reviewed the manuscript. All authors have read and approved the final manuscript.

Notes

The authors declare no competing financial interest.

■ ACKNOWLEDGMENTS

This work was financially supported by IKERBASQUE-Basque Foundation for Science, MINECO (RTI2018-098951−B-I00), the Basque Health Department (projects 2022333035, 2022333039, and 2022333031), the University of the Basque Country (projects COLLAB22/05 and GIU21/033), and the Ministry of Science and Innovation of the Government of Spain (project PID2020-114356RB-I00). The authors thank Elettra Synchrotron for beamtime allocation and acknowledge the CERIC−ERIC Consortium for the access (20212178) to experimental facilities. S.E.M. thanks the PID2020-114356RB-I00 project from the Ministry of Science and Innovation of the Government of Spain. This work was performed under the Maria de Maeztu Units of Excellence Program from the Spanish State Research Agency - Grant no. MDM-2017-0720. K.K. thanks JdC Grant FJC2021-047607-I funded by MCIN/AEI/10.13039/501100011033. The authors thank for the support provided by SGIker (UPV/EHU/ERDF, EU) for the measurements of NMR. The authors gratefully thank Desirè Di Silvio, Loli Martin, Marta Gallego, and Marco Möller for their help in the microscopy analysis, and Jakes Udabe for proofreading the manuscript. We also thank Alejandro J. Müller for the help in the calorimetry measurements.

■ REFERENCES

(1) Banik, B. L.; Fattahi, P.; Brown, J. L. Polymeric nanoparticles: the future of nanomedicine. *Wiley Interdiscip Rev. Nanomed Nanobiotechnol* **2016**, *8*, 271−299.

(2) Abdel-Mageed, H. M.; AbuelEzz, N. Z.; Radwan, R. A.; Mohamed, S. A. Nanoparticles in nanomedicine: a comprehensive updated review on current status, challenges and emerging opportunities. *J. Microencapsulation* **2021**, *38*, 414−436.

(3) Karg, M.; Pich, A.; Hellweg, T.; Hoare, T.; Lyon, L. A.; Crassous, J. J.; Suzuki, D.; Gumerov, R. A.; Schneider, S.; Potemkin, I. I.; Richtering, W. Nanogels and Microgels: From Model Colloids to Applications, Recent Developments, and Future Trends. *Langmuir* **2019**, *35*, 6231−6255.

(4) Cautela, J.; Stenqvist, B.; Schillén, K.; Belić, D.; Månsson, L. K.; Hagemans, F.; Seuss, M.; Fery, A.; Crassous, J. J.; Galantini, L. Supracolloidal Atomium. *ACS Nano* **2020**, *14* (11), 15748−15756.

(5) Cautela, J.; Lattanzi, V.; Månsson, L. K.; Galantini, L.; Crassous, J. J. Sphere−Tubule Superstructures through Supramolecular and Supracolloidal Assembly Pathways. *Small* **2018**, *14* (50), 1803215.

(6) Kaewruethai, T.; Laomeephol, C.; Pan, Y.; Luckanagul, J. A. Multifunctional polymeric nanogels for biomedical applications. *Gels* **2021**, *7*, 228−18.

(7) Anooj, E. S.; Charumathy, M.; Sharma, V.; Vibala, B. V.; Gopukumar, S. T.; Jainab, S. I. B.; Vallinayagam, S. Nanogels: An overview of properties, biomedical applications, future research trends and developments. *J. Mol. Struct.* **2021**, *1239*, No. 130446.

(8) Asadian-Birjand, M.; Sousa-Herves, A.; Steinhilber, D.; Cuggino, J. C.; Calderon, M. Functional Nanogels for Biomedical Applications. *Curr. Med. Chem.* **2012**, *19*, 5029−5043.

(9) Kandil, R.; Merkel, O. M. Recent progress of polymeric nanogels for gene delivery. *Curr. Opin. Colloid Interface Sci.* **2019**, *39*, 11−23.

(10) Mauri, E.; Perale, G.; Rossi, F. Nanogel Functionalization: A Versatile Approach to Meet the Challenges of Drug and Gene Delivery. *ACS Appl. Nano Mater.* **2018**, *1*, 6525−6541.

(11) Suhail, M.; Rosenholm, J. M.; Minhas, M. U.; Badshah, S. F.; Naeem, A.; Khan, K. U.; Fahad, M. Nanogels as drug-delivery systems: a comprehensive overview. *Therapeutic Delivery* **2019**, *10*, 697−717.

(12) Ahmed, S.; Alhareth, K.; Mignet, N. Advancement in Nanogel formulations provides controlled drug release. *Int. J. Pharm.* **2020**, *584*, No. 119435.

(13) Sun, H.; Jiang, C.; Wu, L.; Bai, X.; Zhai, S. Cytotoxicity-Related Bioeffects Induced by Nanoparticles: The Role of Surface Chemistry. *Front. Bioeng. Biotechnol.* **2019**, *7*, 414.

(14) Spencer, D. S.; Shodeinde, A. B.; Beckman, D. W.; Luu, B. C.; Hodges, H. R.; Peppas, N. A. Cytocompatibility, membrane disruption, and siRNA delivery using environmentally responsive cationic nanogels. *J. Controlled Release* **2021**, *332*, 608−619.

(15) Desai, P.; Rimal, R.; Florea, A.; Gumerov, R. A.; Santi, M.; Sorokina, A. S.; Sahnoun, S. E. M.; Fischer, T. M.; Mottaghy, F. M.; Morgenroth, A.; Mourran, A.; Potemkin, I. I.; Möller, M.; Singh, S. Tuning the Elasticity of Nanogels Improves Their Circulation Time by Evading Immune Cells. *Angew. Chem. - Int. Ed.* **2022**, *61*, No. e202116653.

(16) Tamura, A.; Oishi, M.; Nagasaki, Y. Enhanced cytoplasmic delivery of siRNA using a stabilized polyion complex based on PEGylated nanogels with a cross-linked polyamine structure. *Biomacromolecules* **2009**, *10*, 1818−1827.

(17) Tamura, A.; Oishi, M.; Nagasaki, Y. Efficient siRNA delivery based on PEGylated and partially quaternized polyamine nanogels: Enhanced gene silencing activity by the cooperative effect of tertiary and quaternary amino groups in the core. *J. Controlled Release* **2010**, *146*, 378−387.

(18) Oishi, M.; Hayashi, H.; Itaka, K.; Kataoka, K.; Nagasaki, Y. pH-Responsive PEGylated nanogels as targetable and low invasive endosomolytic agents to induce the enhanced transfection efficiency of nonviral gene vectors. *Colloid Polym. Sci.* **2007**, *285*, 1055−1060.

(19) Espuche, B.; Moya, S. E.; Calderon, M. Nanogels: Smart tools to enlarge the therapeutic window of gene therapy. *Int. J. Pharm.* **2024**, *653*, No. 123864.
(20) Li, C.; Obireddy, S. R.; Lai, W. F. Preparation and use of nanogels as carriers of drugs. *Drug Deliv* **2021**, *28*, 1594−1602.
(21) Zhang, R.; Gao, R.; Gou, Q.; Lai, J.; Li, X. Precipitation Polymerization: A Powerful Tool for Preparation of Uniform Polymer Particles. *Polymers* **2022**, *14* (9), 1851.
(22) Ramli, R. A.; Laftah, W. A.; Hashim, S. Core-shell polymers: A review. *RSC Adv.* **2013**, *3*, 15543−15565.
(23) Li, W. H.; Stöver, H. D. H. Monodisperse cross-linked core-shell polymer microspheres by precipitation polymerization. *Macromolecules* **2000**, *33*, 4354−4360.
(24) Blackburn, W. H.; Lyon, L. A. Size-controlled synthesis of monodisperse core/shell nanogels. *Colloid Polym. Sci.* **2008**, *286*, 563−569.
(25) Zha, L.; Banik, B.; Alexis, F. Stimulus responsive nanogels for drug delivery. *Soft Matter* **2011**, *7*, 5908−5916.
(26) Wang, H.; Gao, L.; Fan, T.; Zhang, C.; Zhang, B.; Al-Hartomy, O. A.; Al-Ghamdi, A.; Wageh, S.; Qiu, M.; Zhang, H. Strategic Design of Intelligent-Responsive Nanogel Carriers for Cancer Therapy. *ACS Appl. Mater. Interfaces* **2021**, *13* (46), 54621−54647.
(27) Molina, M.; Giulbudagian, M.; Calderón, M. Positively charged thermoresponsive nanogels for anticancer drug delivery. *Macromol. Chem. Phys.* **2014**, *215*, 2414−2419.
(28) Witting, M.; Molina, M.; Obst, K.; Plank, R.; Eckl, K. M.; Hennies, H. C.; Calderón, M.; Frieß, W.; Hedtrich, S. Thermosensitive dendritic polyglycerol-based nanogels for cutaneous delivery of biomacromolecules. *Nanomedicine* **2015**, *11*, 1179−1187.
(29) Theune, L. E.; Charbaji, R.; Kar, M.; Wedepohl, S.; Hedtrich, S.; Calderón, M. Critical parameters for the controlled synthesis of nanogels suitable for temperature-triggered protein delivery. *Materials Science and Engineering C* **2019**, *100*, 141−151.
(30) Miceli, E.; Wedepohl, S.; Osorio Blanco, E. R.; Rimondino, G. N.; Martinelli, M.; Strumia, M.; Molina, M.; Kar, M.; Calderón, M. Semi-interpenetrated, dendritic, dual-responsive nanogels with cytochrome c corona induce controlled apoptosis in HeLa cells. *Eur. J. Pharm. Biopharm.* **2018**, *130*, 115−122.
(31) Keerl, M.; Pedersen, J. S.; Richtering, W. Temperature sensitive copolymer microgels with nanophase separated structure. *J. Am. Chem. Soc.* **2009**, *131*, 3093−3097.
(32) Cuggino, J. C.; Alvarez I., C. I.; Strumia, M. C.; Welker, P.; Licha, K.; Steinhilber, D.; Mutihac, R. C.; Calderón, M. Thermosensitive nanogels based on dendritic polyglycerol and N-isopropylacrylamide for biomedical applications. *Soft Matter* **2011**, *7*, 11259−11266.
(33) Haider, R.; Sartori, B.; Radeticchio, A.; Wolf, M.; Dal Zilio, S.; Marmiroli, B.; Amenitsch, H. μDrop: a system for high-throughput small-angle X-ray scattering measurements of microlitre samples. *J. Appl. Crystallogr.* **2021**, *54*, 132−141.
(34) Burian, M.; Marmiroli, B.; Radeticchio, A.; Morello, C.; Naumenko, D.; Biasiol, G.; Amenitsch, H. Picosecond pump−probe X-ray scattering at the Elettra SAXS beamline. *J. Synchrotron Radiat.* **2020**, *27*, 51−59.
(35) Beaucage, G. Small-Angle Scattering from Polymeric Mass Fractals of Arbitrary Mass-Fractal Dimension. *J. Appl. Co,st* **1996**, *29*, 134−146.
(36) Spinozzi, F.; Ferrero, C.; Ortore, M. G.; De Maria Antolinos, A.; Mariani, P. GENFIT: Software for the analysis of small-angle X-ray and neutron scattering data of macro-molecules in solution. *J. Appl. Crystallogr.* **2014**, *47*, 1132−1139.
(37) Osorio-Blanco, E. R.; Bergueiro, J.; Abali, B. E.; Ehrmann, S.; Böttcher, C.; Müller, A. J.; Cuéllar-Camacho, J. L.; Calderón, M. Effect of Core Nanostructure on the Thermomechanical Properties of Soft Nanoparticles. *Chem. Mater.* **2020**, *32*, 518−528.
(38) Smith, M. H.; Herman, E. S.; Lyon, L. A. Network Deconstruction Reveals Network Structure in Responsive Microgels. *J. Phys. Chem. B* **2011**, *115* (14), 3761−3764.
(39) Hasegawa, U.; Sawada, S.-I.; Shimizu, T.; Kishida, T.; Otsuji, E.; Mazda, O.; Akiyoshi, K. Raspberry-like assembly of cross-linked nanogels for protein delivery. *J. Controlled Release* **2009**, *140*, 312−317.
(40) Zou, H.; Zhai, S. Synthetic strategies for raspberry-like polymer composite particles. *Polym. Chem.* **2020**, *11*, 3370−3392.
(41) Wellert, S.; Radulescu, A.; Carl, A.; Klitzing, R., Von; Gawlitza, K. Evolution of Size and Structure during the Polymerization Process: A SANS Study on EG-Based Microgels. *Macromolecules* **2015**, *48*, 4901−4909.
(42) Raup, A.; Stahlschmidt, U.; Jérâme, V.; Synatschke, C.; Müller, A.; Freitag, R. Influence of polyplex formation on the performance of star-shaped polycationic transfection agents for mammalian cells. *Polymers* **2016**, *8*, 224.
(43) van de Wetering, P.; Cherng, J. Y.; Talsma, H.; Crommelin, D. J. A.; Hennink, W. E. 2- (dimethylamino) ethyl methacrylate based (co) polymers as gene transfer agents. *J. Controlled Release* **1998**, *53*, 145−153.
(44) Hinrichs, W. L. J.; Schuurmans-Nieuwenbroek, N. M. E.; van de Wetering, P.; Hennink, W. E. Thermosensitive polymers as carriers for DNA delivery. *J. Controlled Release* **1999**, *60*, 249−259.
(45) Chen, Z.; Song, X.; Soh, W. W. M.; Wen, Y.; Zhu, J.; Zhang, M.; Li, J. In Situ Synthesis of Magnetic Poly(DMAEAB-co-NIPAm)@Fe_3O_4 Composite Hydrogel for Removal of Dye from Water. *Gels* **2021**, *7* (4), 201.
(46) Virtanen, J.; Tenhu, H. Studies on Copolymerization of N-Isopropylacrylamide and Glycidyl Methacrylate. *J. Polym. Sci. Part A* **2001**, *39* (21), 3716−3725.
(47) Muzammil, E. M.; Khan, A.; Stuparu, M. C. Post-polymerization modification reactions of poly(glycidyl methacrylate)s. *RSC Adv.* **2017**, *7*, 55874−55884.
(48) Vdovchenko, A.; Pearce, A. K.; Freeley, M.; O'Reilly, R. K.; Resmini, M. Effect of heterogeneous and homogeneous polymerisation on the structure of pNIPAm. nanogels. *Polym. Chem.* **2021**, *12*, 6854−6864.
(49) Di Consiglio, M.; Sturabotti; Brugnoli, B.; Piozzi, A.; Migneco, L. M.; Francolini, L. Synthesis of sustainable eugenol/hydroxyethyl-methacrylate-based polymers with antioxidant and antimicrobial properties. *Polym. Chem.* **2023**, *14*, 432−442.
(50) Garcia, H.; Barros, A. S.; Goncalves, C.; Gama, F. M.; Gil, A. M. Characterization of dextrin hydrogels by FTIR spectroscopy and solid state NMR spectroscopy. *Eur. Polym. J.* **2008**, *44* (7), 2318−2329.
(51) Magonov, S. N.; Elings, V.; Whangbo, M. H. Phase imaging and stiffness in tapping-mode atomic force microscopy. *Surf. Sci. Lett.* **1997**, *375*, L385−L391.
(52) Stark, M.; Möller, C.; Müller, D. J.; Guckenberger, R. From Images to Interactions: High-Resolution Phase Imaging in Tapping-Mode Atomic Force Microscopy. *Biophys. J.* **2001**, *80*, 3009.
(53) Rancan, F.; Asadian-Birjand, M.; Dogan, S.; Graf, C.; Cuellar, L.; Lommatzsch, S.; Blume-Peytavi, U.; Calderón, M.; Vogt, A. Effects of thermoresponsivity and softness on skin penetration and cellular uptake of polyglycerol-based nanogels. *J. Controlled Release* **2016**, *228*, 159−169.
(54) Richter, M.; Steinhilber, D.; Haag, R.; Von Klitzing, R. Visualization of real-time degradation of pH-responsive polyglycerol nanogels via atomic force microscopy. *Macromol. Rapid Commun.* **2014**, *35*, 2018−2022.
(55) Giulbudagian, M.; Hönzke, S.; Bergueiro, J.; Işık, D.; Schumacher, F.; Saeidpour, S.; Lohan, S. B.; Meinke, M. C.; Teutloff, C.; Schäfer-Korting, M.; Yealland, G.; Kleuser, B.; Hedtrich, S.; Calderón, M. Enhanced topical delivery of dexamethasone by β-cyclodextrin decorated thermoresponsive nanogels. *Nanoscale* **2018**, *10*, 469−479.
(56) Schulte, M. F.; Scotti, A.; Gelissen, A. P. H.; Richtering, W.; Mourran, A. Probing the Internal Heterogeneity of Responsive Microgels Adsorbed to an Interface by a Sharp SFM Tip: Comparing Core-Shell and Hollow Microgels. *Langmuir* **2018**, *34*, 4150−4158.
(57) Müller, M.; Urban, B.; Reis, B.; Yu, X.; Grab, A.; Cavalcanti-Adam, E.; Kuckling, D. Switchable release of bone morphogenetic

https://doi.org/10.1021/acs.macromol.4c00350
Macromolecules 2024, 57, 6035−6048

protein from thermoresponsive poly(NIPAM-co-DMAEMA)/cellulose sulfate particle coatings. *Polymers* **2018**, *10*, 1314.
(58) Moselhy, J.; Vira, T.; Liu, F. F.; Wu, X. Y. Characterization of complexation of poly (N-isopropylacrylamide-co-2-(dimethylamino) ethyl methacrylate) thermoresponsive cationic nanogels with salmon sperm DNA. *Int. J. Nanomedicine* **2009**, *4*, 153−164.
(59) Martinez-Moro, M.; Jenczyk, J.; Giussi, J. M.; Jurga, S.; Moya, S. E. Kinetics of the thermal response of poly (N-isopropylacrylamide co methacrylic acid) hydrogel microparticles under different environmental stimuli: A time-lapse NMR study. *J. Colloid Interface Sci.* **2020**, *580*, 439−448.

https://doi.org/10.1021/acs.macromol.4c00350
Macromolecules 2024, 57, 6035−6048